RESEARCH ARTICLE | OCTOBER 17 2023

Spectral insight into the interface evolution of a carbon/carbon composite under high-enthalpy, nonequilibrium flow ⊘

Sihan Fang (方思晗) ; Xin Lin (林鑫) ✉ ; Junna Yang (杨俊娜); Hui Zeng (曾徽) ; Xingying Zhu (朱兴营);
Fa Zhou (周法); Dongbin Ou (欧东斌); Fei Li (李飞) ; Xilong Yu (余西龙)

Check for updates

View Online

Export Citation

Physics of Fluids

Special Topic:
Flow and Civil Structures

Submit Today

AIP Publishing

AIP Publishing

Spectral insight into the interface evolution of a carbon/carbon composite under high-enthalpy, nonequilibrium flow

View Online   Export Citation   CrossMark

Sihan Fang (方思晗),[1,2] [iD] **Xin Lin** (林鑫),[1,a] [iD] **Junna Yang** (杨俊娜),[1,2] **Hui Zeng** (曾徽),[3] [iD] **Xingying Zhu** (朱兴营),[3] **Fa Zhou** (周法),[3] **Dongbin Ou** (欧东斌),[3] **Fei Li** (李飞),[1] [iD] and **Xilong Yu** (余西龙)[1,2]

AFFILIATIONS

[1]State Key Laboratory of High Temperature Gas Dynamics, Institute of Mechanics, Chinese Academy of Sciences, Beijing 100190, China
[2]School of Engineering Science, University of Chinese Academy of Sciences, Beijing 100049, China
[3]China Academy of Aerospace Aerodynamics, Beijing 100074, China

[a]Author to whom correspondence should be addressed: linxin_bit@imech.ac.cn

ABSTRACT

Gas–surface interactions between thermal protection materials and high-enthalpy nonequilibrium flow are one of the greatest challenges in accurately predicting aerodynamic heating during supersonic flights. Finer microscopic details of flow properties are required for elaborate simulation of these interactions. Spectral insight, with quantum-state-specific characteristics, is provided in this work to investigate the physico-chemical processes in high temperature interface of a carbon/carbon (C/C) composite. The nonequilibrium air flow is produced by a 1.2 MW inductively coupled plasma wind tunnel at an enthalpy of 20.08 MJ/kg. The duration of each test is up to 100 s, and quartz is also tested for comparison. Spectral insights into the reaction mechanisms of the gas–surface interactions are acquired by the optical emission spectroscopy and laser absorption spectroscopy. Dynamic evolution of the chemical reaction pathways and thermal nonequilibrium are discussed based on the results of optical emission spectroscopy. Temporally and spatially resolved results of the translational temperature and number density of atomic oxygen are quantified by laser absorption spectroscopy. Controlling mechanisms in the surface chemistry are further analyzed in conjunction with the surface temperature, scanning electron microscopy, and energy dispersive spectroscopy. Reaction mechanisms on the C/C composite surface sequentially experience an oxidation-dominant, an intense competitive, a nitridation-dominant, and a recession dominant period. Distributions in the axial direction and dynamic characteristics of the translational temperature and number density of atomic oxygen are found closely related with surface swelling, recession, and chemical reactions. The results herein are consistent with each other and are instructive to further investigate the interface evolution on C/C composites.

NOMENCLATURE

A_{ul}	Einstein coefficient (s^{-1})
A_{int}	Integrated absorbance (cm^{-1})
c	Light velocity (m/s)
E_l	Lower state energy (eV)
$F(v',J')$	Rotational energy (J)
$G(v')$	Vibrational energy (J)
g_l	Lower state degeneracy
g_u	Upper state degeneracy
$I^{v',J'}_{v'',J''}$	Emission intensity
k	Boltzmann constant (J/K)
k_v	Absorption coefficient (cm^{-1})
L	Absorption length (cm)
M	Atomic mass (kg/mol)
n_l	lower state number density (cm^{-1})
Q_{el}	Electronic partition function of an atom
Q_{el}^{O}	Electronic partition function of atomic oxygen
$S_{J''}^{J'}$	Hönl–London factor
T_{LTE}	Temperature at the LTE (K)
T_{rot}	Rotational temperature (K)
T_S	Surface temperature (K)
T_{tr}	Translational temperature (K)
T_{vib}	Vibrational temperature (K)

x	Distance from the stagnation point (mm)0
Δv_D	Doppler broadening (cm^{-1})
λ_0	Central wavelength of the transition (nm)
v	Wavenumber (cm^{-1})
v_0	Central wavenumber (cm^{-1})
(v',J')	Vibrational and rotational quantum numbers in the upper level
(v'',J'')	Vibrational and rotational quantum numbers in the lower level

I. INTRODUCTION

Carbon/carbon (C/C) composite is one of the most promising high temperature thermal protection materials for supersonic heat shielding applications.[1,2] Due to their exceptional advantages of chemical and thermal resistance, excellent mechanical properties at elevated temperature as well as low densities,[3–7] C/C composites, are used to equip at high temperature regions such as the nose tips and wing leading edges.[8–11]

Further applications of C/C composites are mainly restricted by incomplete knowledge of the gas–surface interactions, which consist of complex physico-chemical processes including sublimation, oxidation, nitridation, and catalysis.[12–18] For the first three reaction types,[5] reactions occur between the flow particles and C/C surface. Products from these reactions couple to the chemically reactive boundary layer, forming a mutually interactive dynamic interface.[17,19] For reactions of catalytic recombination, C/C surface serves as a catalyst to trigger the catalytic recombination between the dissociated atoms.[20,21] The chemical energy released from these catalytic reactions strongly augments the aerothermal heating.[22] All these reactions substantially alter the surface properties and the heat flux.[2] It can be concluded that gas–surface interactions are involved with multi-field coupling (of thermal–mechanical–chemical processes) and multi-scale coupling (of macroscopic flow structure and microscopic reactions).[17,23] Current simulation works have difficulty to accurately predict the properties of the interface. Experimental investigations are, therefore, essential because they can directly reflect the elementary processes of the interface.

Past experimental efforts to characterize gas–surface interactions of carbon-based materials mainly used two approaches: non-spectroscopic and spectroscopic. In the non-spectroscopic approach, the oxidation behavior or catalytic effect of the material was generally characterized by the surface temperature, recession rate, and heat flux.[7] Comparisons were made between various heating conditions, exposure times, and material types to analyze the controlling factors of the thermal response. In this approach, analysis of the reaction mechanisms and corresponding parameters, such as the oxidation rate, strongly depended on comparisons[2,24] or combinations[6,20,25] with numerical simulations. This might lead to unphysical results because of the assumptions in simulations.[20] Additionally, this approach limited the analysis of interactions to a speculative description. Important parameters that are directly related to the reaction mechanisms, such as the plasma temperature, atomic number density, and emission characteristics, are, therefore, needed.[26]

Macroscopic observations of the physical world regarding gas–surface interactions directly associate with the microscopic world of transitions between quantum-states. A spectroscopic approach, with quantum-state-specific characteristics, can provide molecular-level

insights into physico-chemical phenomena. Optical emission spectroscopy (OES) and two-photon absorption laser-induced fluorescence (TALIF) are two major techniques in spectroscopic approach. Based on the relationship between the atomic number density and intensity of the signal, both techniques aimed to inform species distributions adjacent to the material surface on a microscopic scale. In most work using OES, analysis was mainly focused on the flow structure of the interface,[10,27,28] the detection ability of OES regarding dynamic changes of the thermal nonequilibrium and reaction processes was not fully used. TALIF was often used to evaluate catalytic properties[21,29] but was rarely used to characterize oxidation in the ablative layer of carbon-based materials. Based on the mass balance assumption between the arriving diffusive flux and the recombination consumption rate, TALIF obtained catalytic efficiency of the targeted species. However, since the conversion of the integrated fluorescence intensity detected by TALIF to the absolute atomic number density required additional complex measurements of the fluorescence lifetime, beam diameter, and detection efficiency,[30] the atomic number density was replaced by the integrated emission intensity, neglecting the coefficient between the number density and integrated emission intensity. Additionally, the bulky and sophisticated experimental equipment of TALIF hindered the development of in-flight sensors for future applications. In OES and TALIF, the problem of directly quantifying the atomic number density is still complicated, particularly in high enthalpy flow. Moreover, these methods lack further applications to the gas–surface interactions on thermal protection materials, especially in large-scale high-enthalpy plasma facilities.

Consequently, to properly characterize the interface evolution on C/C composite, accurate detection of the quantitative number density and its dynamic variations under the high-enthalpy supersonic flow is paramount. For thermochemistry investigations of reactive flows, laser absorption spectroscopy (LAS) is a promising technique for quantifying the ground-state number density of targeted atoms and molecules under extreme conditions. Due to its advantages of high fidelity, fast response, robustness, and compactness,[31–33] LAS has been applied to characterize the performance of plasma flow properties,[34] atmospheric monitoring,[35] engines,[36–38] and coal gasifiers[39] over the past two decades. Considering the direct relationship to reactive nature of the gas–surface interactions concerned in this study,[40] OES is combined with LAS to propose an OES/LAS method, enabling both the qualitative multiple-species sensing and quantitative species-selective sensing under high-enthalpy flow. The feasibility of this coupled spectral method has been identified in a high-temperature interface on a silicon carbide surface in our previous study.[41]

In this study, a deeper understanding of the gas–surface interactions on a C/C composite is achieved based on spectroscopic insights by OES/LAS method. High enthalpy, nonequilibrium flow is provided by a 1.2 MW inductively coupled plasma (ICP) wind tunnel at the China Academy of Aerospace Aerodynamics (CAAA),[41] with the stagnation enthalpy of 20.08 MJ/kg. The duration of each test is up to 100 s to investigate the dynamic characteristics of the interactions. Quartz is also tested for comparison because of its relatively low reactivity.[42] To reveal the reaction mechanisms and thermal nonequilibrium state on a molecular scale, dynamic variations of emission spectra from important reaction particles are identified by OES. Spectral insights of the chemical behavior of atomic oxygen and its relationship to surface variations are provided by quantitative results of the translational

08 April 2024 02:59:17

temperature and number density through LAS. Finally, controlling mechanisms of the surface chemistry are discussed in combination with the surface temperature, scanning electron microscopy (SEM), and energy dispersive spectroscopy (EDS).

II. STRATEGY FOR PROVIDING SPECTRAL INSIGHTS

Details of our strategy are introduced as shown in Fig. 1. It consists of two parts: spectroscopic and traditional measurements. The former, including OES and LAS, provides spectral insights into the interactions, which informs the reaction behavior of the excited particles. The latter provides a macroscopic perspective of the high-temperature interface. In spectroscopic measurements, OES simultaneously records the emission spectra over a wide wavelength range and finer spectra in a specific range. The former spectra characterize dynamic trends of multiple species for identifying the dominant reaction mechanisms. The latter determines rotational temperature (T_{rot}) and vibrational temperature (T_{vib}) in combination with simulated spectra based on the OES theory: Assuming the energy levels follow a Boltzmann distribution, the emission intensity can be described by

$$I^{v',J'}_{v'',J''} \propto \left(v^{v',J''}_{v'',J''} \right)^4 S^{J'}_{J''} \exp\left(-\frac{F(v',J')}{kT_r} - \frac{G(v')}{kT_v} \right). \tag{1}$$

Spectroscopic parameters in this equation are listed in the Nomenclature and detailed information regarding OES theory is presented in Ref. 43.

Time series of raw LAS signals adjacent to the sample surface depicts the dynamic profile variations including swelling and recession. Additionally, quantitative results of the translational temperature and atomic number density reveal the elaborate reaction processes at the interface. In this work, the transition line of atomic oxygen from $3s^5S^0_2$ to $3p^5P_{3,2,1}$ at the wavelength of 777.19 nm is chosen,[2,6,25,44,45] the

reasons for which are discussed in our previous work.[41] Some of the important expressions in LAS are succinctly presented here as an illustration. The Doppler broadening under this condition is estimated to be nearly three orders of magnitude larger than the Stark broadening (at n_e of 10^{13} cm^3).[41] Hence, the T_{tr} (assumed to be equal to the local excitation temperature) is obtained from Doppler broadening in the detected absorption profile[46,47]

$$\Delta v_D = 7.1623 \times 10^{-7} v_0 \sqrt{T_{tr}/M}, \tag{2}$$

where Δv_D (cm^{-1}) is the Doppler broadening, v_0 (cm^{-1}) is the central wavenumber of the transition, and M is the atomic mass of the targeted species. The number density of the atom was then obtained from the integrated absorbance A_{int} (cm^{-1}) (which is deduced from the Doppler profile fitting)

$$n_l = \frac{A_{int}}{\lambda_0^4 L(g_u/g_l)(A_{ul}/8\pi c)} = \frac{\int k_v dv}{\lambda_0^4 (g_u/g_l)(A_{ul}/8\pi c)}, \tag{3}$$

where n_l (cm^{-3}) is the lower state number density of the atom, λ_0 (nm) is the central wavelength of the transition, L (cm) is the absorption length, g_l is the lower state degeneracy, g_u is the upper state degeneracy, A_{ul} (s^{-1}) is the Einstein coefficient of the transition, c (cm/s) is the light velocity, and k_v (cm^{-1}) is the absorption coefficient at the frequency v (s^{-1}). For gases assumed to be in local thermodynamic equilibrium (LTE), the lower state number density n_l is converted into the total number density n_O by using the Boltzmann distribution[48–52]

$$\frac{n_l}{n_O} = \frac{g_l}{Q_O} \exp\left(-\frac{E_l}{k_B T} \right), \tag{4}$$

where E_l is the lower state energy and Q_O is the electronic partition function of atomic oxygen. Theoretically, the partition function is
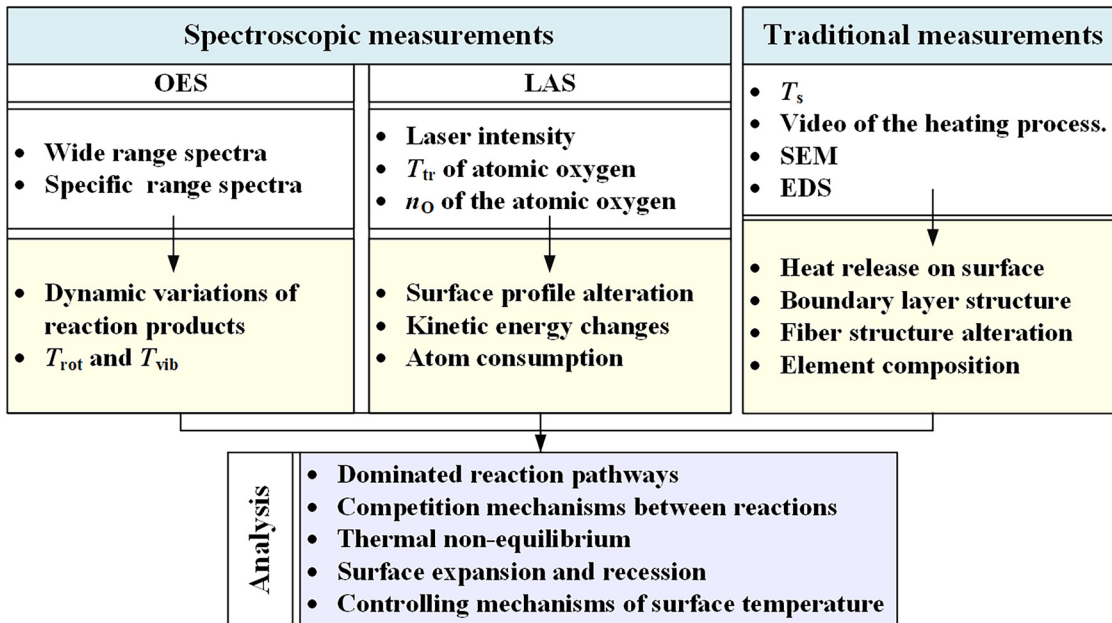

Spectroscopic measurements		Traditional measurements
OES	**LAS**	• T_s • Video of the heating process. • SEM • EDS
• Wide range spectra • Specific range spectra	• Laser intensity • T_{tr} of atomic oxygen • n_O of the atomic oxygen	
• Dynamic variations of reaction products • T_{rot} and T_{vib}	• Surface profile alteration • Kinetic energy changes • Atom consumption	• Heat release on surface • Boundary layer structure • Fiber structure alteration • Element composition

Analysis
• Dominated reaction pathways
• Competition mechanisms between reactions
• Thermal non-equilibrium
• Surface expansion and recession
• Controlling mechanisms of surface temperature

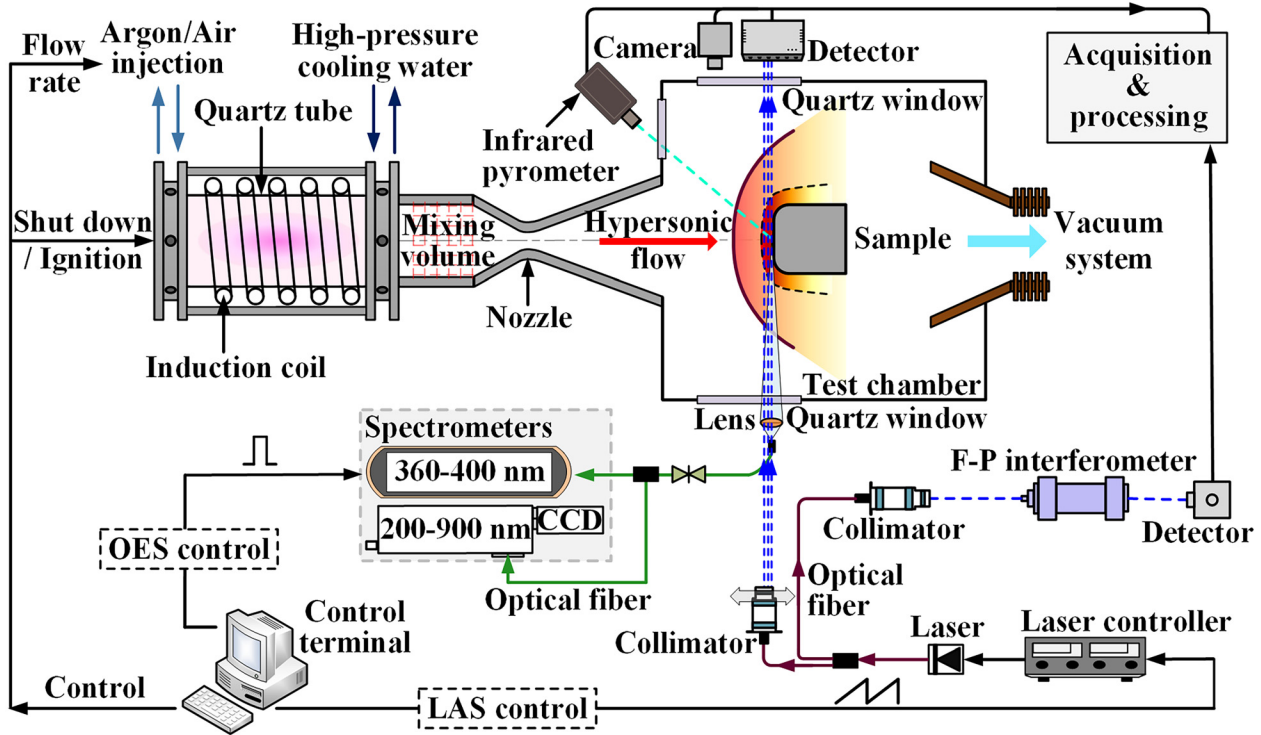**FIG. 1.** Schematic of the strategy for obtaining the spectral insights.

FIG. 2. Schematic of the experimental setup of the 1.2 MW wind tunnel at the CAAA (not to scale). LAS: laser absorption spectroscopy. OES: optical emission spectroscopy. CCD: charge-coupled device camera.

defined as a function of each energy level j and temperature at the LTE, T_{LTE}[48,53]

$$Q_{el} = \sum_{j}^{\infty} g_j \exp\left(-\frac{E_j}{k_B T_{LTE}}\right). \tag{5}$$

Here, the electronic partition function of atomic oxygen is written as limited expansions of several levels[54–56]

$$Q_{el}^{\text{O}}(T) = 5 + 3\exp(-228/T_{LTE}) + \exp(-326/T_{LTE})$$
$$+ O(\exp(-23000/T_{LTE})). \tag{6}$$

To capture additional information of the highly reactive boundary layer, traditional measurements including surface temperature, video records, SEM, and EDS are also used. Finally, the OES/LAS method is expected to reveal complex mechanisms of the dominant reaction pathways, reaction processes, thermal nonequilibrium, surface swelling, and recession as well as their relationships to the surface temperature of the C/C composite.

III. EXPERIMENTAL SETUP

The gas–surface interactions of the C/C composite are investigated in a supersonic plasma flow produced by the 1.2 MW ICP wind tunnel at CAAA, a schematic view of the experimental setup for *in situ* measurements is shown in Fig. 2. The entire experimental system consists of four subsystems: the ICP wind tunnel system, optical diagnostic system, surface temperature, and video records and test specimens.

A. 1.2 MW ICP wind tunnel

The ICP wind tunnel consists of an ICP torch, a supersonic nozzle, a test chamber, and a vacuum system. The ICP torch is powered by a high-frequency (400 kHz), high-power (1.2 MW), and high-voltage (2 kV) generator; enabling long-duration high-enthalpy plasma heating (up to tens of minutes). Before the air injection, argon is introduced and discharged to form a high degree of ionization. This ionization increases the density of plasma electrons and electrical conductivity of plasma, which make it easier to dissociate the air.[57] Standard air (79% N_2 and 21% O_2) is radially injected into the ICP generator. The gas is compressed and expanded through the nozzle, generating a high enthalpy plasma flow. Flow conditions are listed in Table I.

TABLE I. Test conditions of the ICP wind tunnel.

Property	Value
Inductive heater power	650.0 kW
Mass flow rate	12.84 g/s
Flow speed	2–2.5 km/s
Mach number	2.1
Static pressure	∼200 Pa
Stagnation enthalpy	20.08 MJ/kg
Heat flux	1.0 MW/m^2

To prevent overheating of the induction coil, high-pressure cooling water is supplied. The test chamber is sufficiently large enough to contain the entire plasma stream. Multiple quartz windows in the chamber wall enable sophisticated and non-intrusive diagnostics. A water-cooled sample holder is installed in a $1.2 \times 1.2 \times 2$ m^3 sized water-cooled test chamber at an axial distance of 140 mm from the nozzle exit. Copper samples in the same configuration are injected into the flow to measure the stagnation pressure and heat flux under the same experimental conditions. When the wind tunnel starts to steadily generate high-enthalpy plasma, the test sample is injected into the plasma flow and is dragged out of the flow before shutting off the wind tunnel.

B. Spectral diagnostic system

The optical pathways of both the OES and LAS system are perpendicular to the centerline of the plasma stream. The acquisition and shut-off of the OES and LAS systems are triggered by a control terminal. The OES system is focused on the optical radiation at the stagnation point with the targeting point of approximately 2 mm. The radiation emitted from the excited particles is collected by a lens (focal length: 1 m), which is then detected by two spectrometers. The adjustable attenuator prevents saturation and, thus, ensures suitable emission intensity. The first type of the spectrometers (Ocean Optics, QE65 Pro) equipped with a charge-coupled device camera (CCD) detects spectra covering a wide wavelength range (200–900 nm) with spectral resolution of 1.2 nm. Another spectrometer (Avantes, AvaSpec-UL2048CL-RS-EVO) records the finer spectra over a narrower wavelength range (360–400 nm) with 3600 lines/mm grating and spectral resolution of 0.06–0.08 nm. The detected emission intensity is calibrated in relative intensity with a NIST traceable quartz–tungsten–halogen standard reference lamp (model 63945, Oriel Instruments, Stratford, CT).

The LAS system consists of the laser emission assembly and detection assembly. Both are mounted onto translational stages (indicated with gray arrows in Fig. 2) to precisely control the axial detection position. In the laser emission assembly, the signal generator (Tektronix, AFG3101) provides a continuous periodic ramp signal at 500 Hz to the laser controller (Thorlabs, model ITC-502). A laser with 0.7–1.0 MHz linewidth (Photodigm, PH778DBR020BF) is modulated by the signal generator and controller through temperature and current control to cover the targeted wavelength at 777.19 nm. The first beam of the laser is directed into the plasma flow through the quartz window. The other beam is directed to a Fabry–Pérot interferometer (Thorlabs, FPSA200-6A-1, 1.5 GHz free spectral range) and, finally, collects with a photodetector (Thorlabs, PDA36A2) to calibrate the absolute wavelength. In the detection assembly, the transmitted laser from the test chamber is collected by a photodetector after focused and filtered by a collimated mirror and a narrow band filter (NBF) with a bandwidth of 10 nm. The signals are detected by the acquisition and processing system through cables at an acquisition rate of 200 kHz. LAS is deployed at various axial distances from the sample surface, enabling spatially resolved detection both adjacent to the surface and in the boundary layer. The centerline of the plasma flow is denoted as the x coordinate. The position at which half of the laser beam is hindered by the sample surface is noted as the starting point of the x coordinate: $x = 0$ mm.

C. Surface temperature and video records

Surface temperature is an important parameter reflecting heat response of the surface on a macroscopic scale. More information regarding reaction mechanisms can be found when spectroscopic measurements are combined with the surface temperature. Surface temperature measurements are carried out using an optical pyrometer (FLUKE Endurance Series, E1MH-F2-L-0-0) allowing detection from 540 to 3000 °C. The temperature data are recorded every 0.1 s with the emissivity and transmissivity set to 0.9 and 1.0, respectively. Calibrations of the pyrometer are performed with a blackbody radiation source. Additionally, a high-definition (HD) digital camera (Canon 5 D Mark III) is used to record the flow structure variations during the entire heating process, and the camera is placed perpendicular to the plasma stream.

D. Test specimens

Figure 3 shows the sample geometry and visual appearance of the tested samples. Both samples feature a cylindrical diameter of 50 mm with a 30 mm-long cylinder and a corner radius of 8 mm. The bottom cylinder attached to the body is designed for sample insertion in the
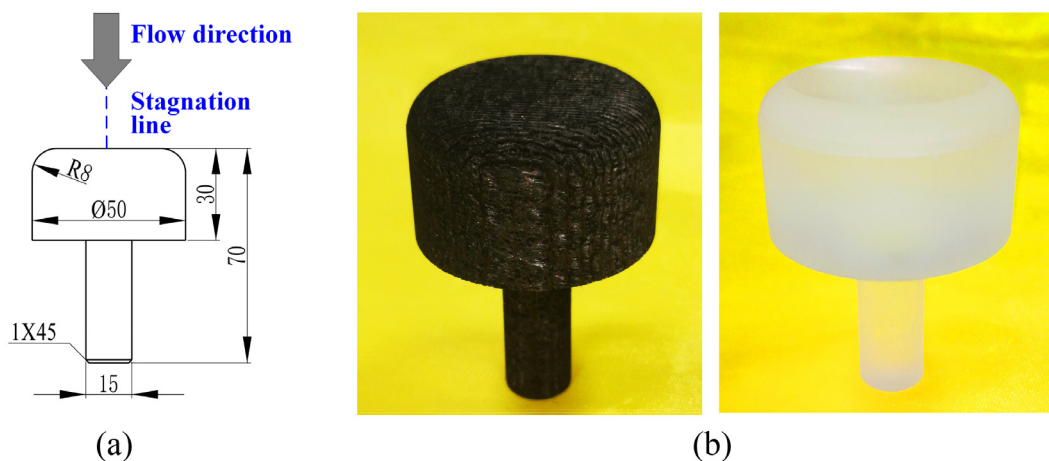
FIG. 3. Shape of the samples: (a) Design graphics and (b) photos of the C/C composite (left) and quartz (right).

holder. Figure 3(a) shows the dimensions of the sample, the plasma stream direction, and the stagnation line coinciding with the plasma flow. The corresponding digital photographs of the samples are shown in Fig. 3(b). Since the C/C composite is manufactured with 2 D needle punching technique, the material surface consists of a net structure with perpendicular-crossed fibers.

IV. RESULTS AND DISCUSSION

A. Video images, surface temperature, and visual inspection

Figure 4 shows snapshots of video records and surface temperature variations during the entire heating period. The C/C composite
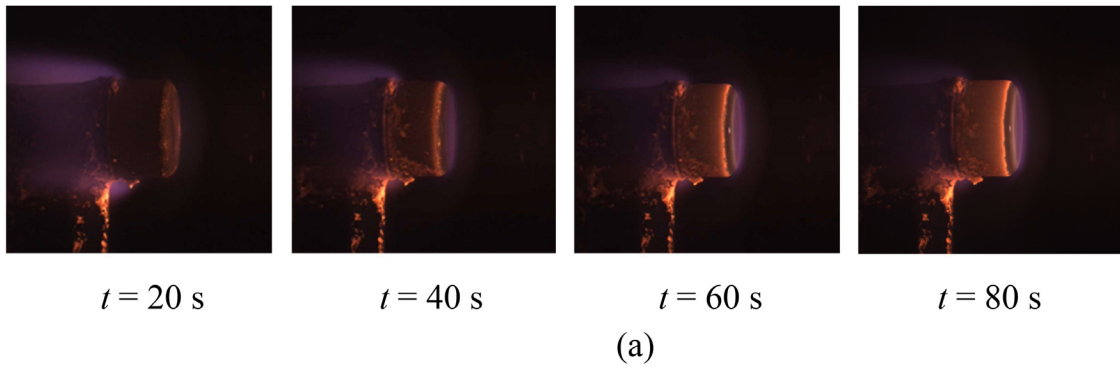

$t = 20$ s $t = 40$ s $t = 60$ s $t = 80$ s

(a)

(b)

$t = 20$ s $t = 40$ s $t = 60$ s $t = 80$ s

(c)
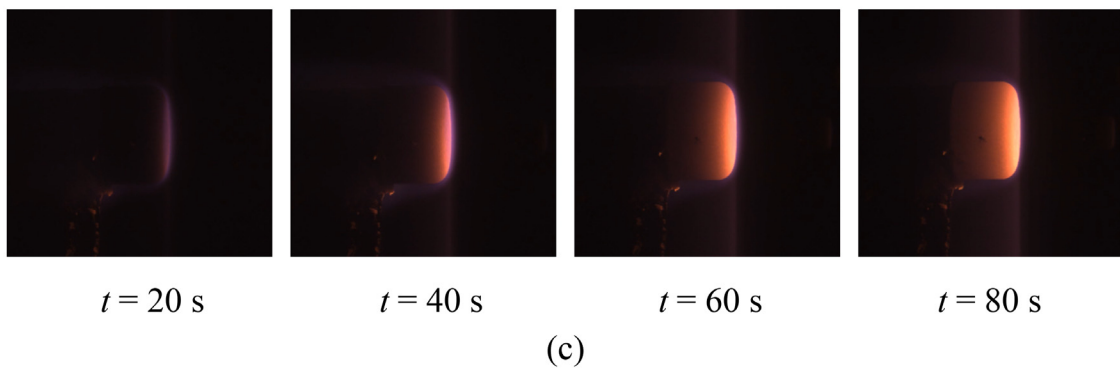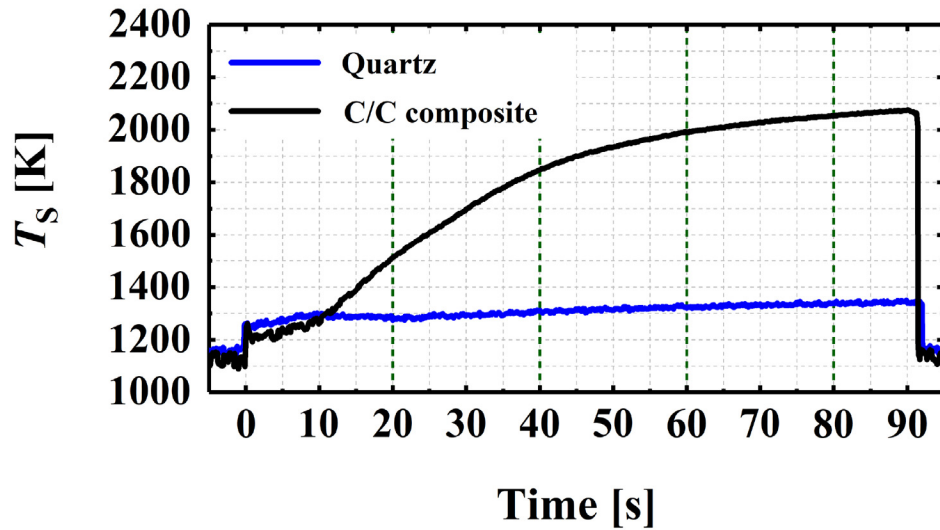
FIG. 4. Video images at critical heating times and time variations of the surface temperature: (a) images of quartz, (b) surface temperature, and (c) images of C/C composite.

and quartz exhibit apparently different temperature responses under the same heating conditions. Regarding the quartz sample (the blue line), the surface temperature abruptly increases to nearly 1300 K as the sample is inserted into the plasma flow. During the following heating process, the variation curve of the surface temperature exhibits a slowly increasing trend, which starts from around 1250 K and finally ends at nearly 1350 K. The transmittance of the quartz surface becomes higher due to surface chemistry as discussed subsequently. The detection spot of the pyrometer is targeted at the cooling holder. Hence, the practical surface temperature on quartz is likely to be higher than the experimental results. Regarding the C/C composite (black line), the surface temperature has a similar abrupt increase as quartz at the sudden sample insertion. After 10 s of plasma heating, the temperature increases around 200 K every 10 s, exceeding 1800 K after heating for 40 s. The increasing rate of the surface temperature on the C/C composite significantly becomes lower with the prolongation of the test time, which gradually reaches a steady state upon a heating time of 80 s. The surface temperature finally reaches 2075 K before the sample is withdrawn from the plasma flow. These temperature results indicate that the C/C composite exhibits a substantially higher increasing rate during the whole heating process and a nearly 700 K higher temperature peak compared with quartz. Such observations are associated with the lower thermal conductivity and higher temperature resistance of the C/C composite compared with quartz,[7] which might result from the higher oxidation/catalytic rate on the C/C surface since most of these reactions are exothermic.

Video snapshots at critical moments during the heating related to surface temperature are shown in Figs. 4(a) and 4(c) for quartz and C/C composite, respectively. Since the HD digital camera is operated in automatic adjustment mode, the radiation brightness in each image does not directly correspond to the temperature. Nevertheless, the brightness pattern distributions in these snapshots still indicate the temperature distributions around and within the sample. The radiation intensity is high at the corner of the quartz sample, which increases slightly in brightness as heating continues. Additionally, the profile of the sample surface gradually becomes increasingly clear, indicating subtle changes in the surface mechanical properties. Regarding the video images of the C/C composite, the radiation intensity changes significantly as the heating proceeds. At the beginning of the plasma heating, the emission intensity is focused at the sample surface. As the heating continued, the brightness patterns significantly increased and rapidly extended axially along the sample surface. The radiation intensity in the boundary layer becomes less than the intensity emitted from C/C surface. Changes in these video images are consistent with the surface temperature variations.
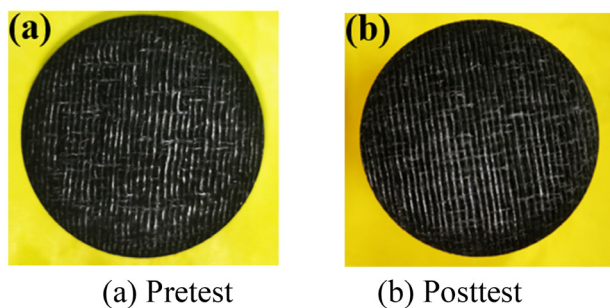

(a) Pretest   (b) Posttest

FIG. 5. Digital photographs of the C/C composite.

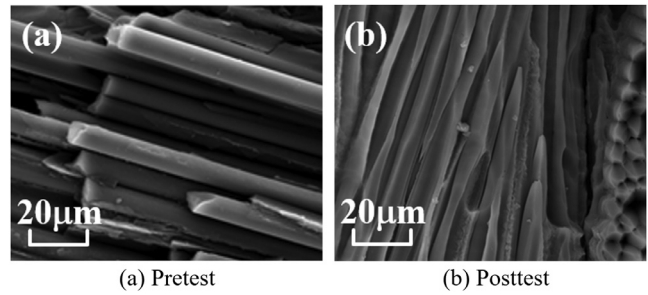(a) Pretest   (b) Posttest

FIG. 6. SEM images of the C/C composite.

Images of the pretest and posttest sample are shown in Fig. 5. Compared with the image of the pretest sample, the posttest image [Fig. 5(b)] shows a slight curvature of the C/C fiber. SEM inspection in Fig. 6 shows substantial thinning of the carbon fibers, creating a larger space interval between the fibers. Additionally, there is a sharp cone feature similar to an icicle shape at the fiber tip. These results are similar to those reported in the research.[10,20] All of these phenomena indicate air ablation on C/C composite during the plasma heating. The EDS results show that the mole fraction of the carbon is larger than 90% both before and after the test, indicating that nearly no particles in the outer gas remain in the C/C fiber layer.

B. Optical emission spectroscopy

1. Emission spectra

Figure 7 shows static spectra in both the wide wavelength range of 200–900 nm and the narrow wavelength range of 360–400 nm during plasma heating. In Fig. 7(a), sharp emission lines of atomic oxygen
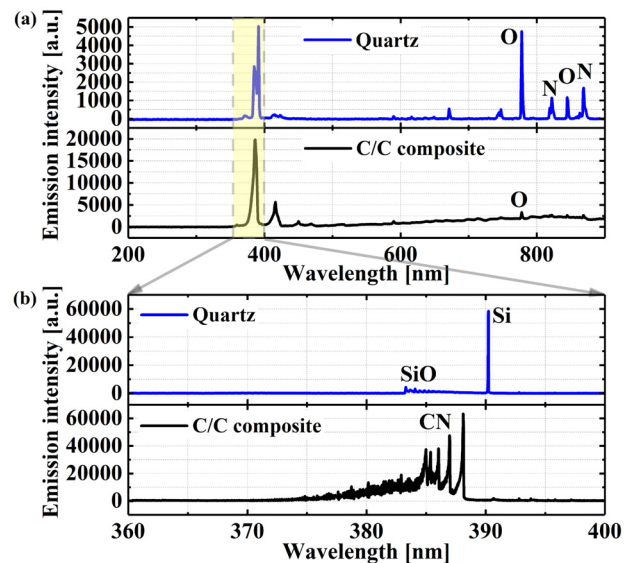

FIG. 7. Emission spectra at the stagnation point: (a) spectra covering the wide wavelength range (200–900 nm) and (b) finer spectra in the ultraviolet spectral region of 360–400 nm.
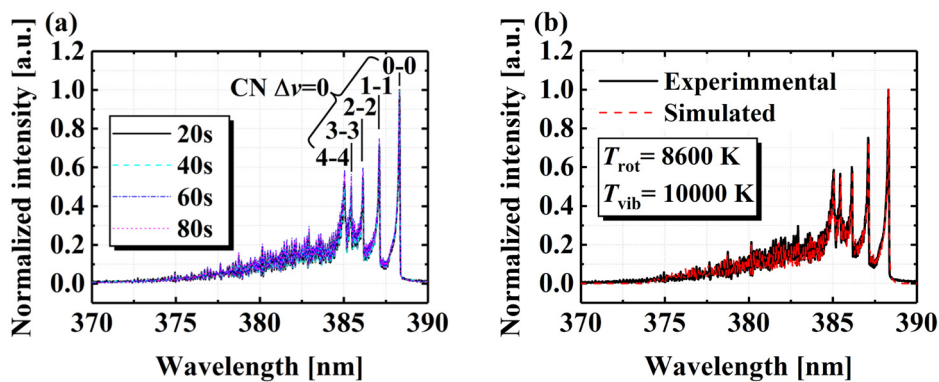
FIG. 8. Spectral structure of CN: (a) Normalized spectra of CN at heating times of 20, 40, 60, and 80 s; (b) T_{rot} and T_{vib} of CN derived from Lifbase.

and nitrogen are detected in the near-infrared region of the quartz sample, indicating that the air was dissociated. For C/C composite, atomic emission lines in the near-infrared region are relatively weaker than that in the ultraviolet region. Finer structure of the spectra in this narrow wavelength range is shown in Fig. 7(b). Strong emission of the silicon (Si) and silicon monoxide (SiO) are evident in the quartz sample; these lines probably originate from sample fabrication and subtle melting, as illustrated in our previous work.[41] For C/C composite, the radiative spectrum is dominated by strong emission of the electronically excited cyanogen (CN) violet $(B^2\sum^+ \rightarrow X^2\sum^+)$ system. CN emission is an important identification of chemical reactions between gases and material surfaces. This product is thought to arise from the mixing and reaction of carbon-rich gas mixtures with excited nitrogen from the shock layer.[10]

2. Rotational temperature T_{rot} and vibrational temperature T_{vib} of CN

Figure 8(a) plots four normalized emission spectra of CN at heating times of 20, 40, 60, and 80 s. The emission intensity remains nearly stable over this heating period, illustrating that the T_{rot} and T_{vib} were stable in the heating period. With a significant increase in the surface temperature, such phenomena might resort to high excitation energy of the rotational and vibrational modes. T_{rot} and T_{vib} of CN are thought to closely reflect the convective heating at the interface. The emission spectra at 60 s are selected to deduce the representative T_{rot} and T_{vib} of CN compared with simulated spectra. T_{rot} and T_{vib} as well as other simulating parameters are adjusted until the synthetic spectra conformed to the experimental one. Finally, T_{rot} is determined to be 8600 K, and T_{vib} is 10 000 K. Measurement uncertainty of T_{rot} and T_{vib} is estimated to be less than 1% and 8%, respectively.[58] This discrepancy between T_{rot} and T_{vib} is indicative of the thermal nonequilibrium in the plasma flow at the interface (further analyzed in the context of the translational temperature of atomic oxygen in Sec. IV C 2). Additionally, the time stability of the temperatures indicates that the dynamic emission intensity of CN directly corresponds to its density variations, which facilitates the subsequent reaction analysis.

3. Chemical reaction mechanisms on C/C composite

Figure 9 shows integrated emission intensity variations of atomic oxygen at 777.19 nm (denoted as O in the following analysis) on quartz surface. Figure 10 shows the variations of O, CN (around 390 nm), and surface temperature on the C/C composite. For quartz sample, the

intensity of atomic oxygen quickly decreases to a stable value after 10 s of heating, showing that the quartz possesses a low reactivity.

The surface temperature strongly affects the chemical reaction rate on C/C composite.[7] At the time of sample insertion, the intensity of O abruptly increases over 10-fold, whereas the intensity of CN exhibits only a slight increase. Such phenomena indicate that the chemical reactivity of O is easily excited since the surface temperature only jumps to around 1200 K. When the surface temperature reaches 1500 K within the initial 20 s of heating, the maximum value of O sharply decreases while the CN intensity gradually increased. These trends indicate that the oxidation reactions are increasingly facilitated; intense chemical interactions emerge between the atomic oxygen and ablative particles in the carbonaceous flow. Simultaneously, the nitridation reactions are somewhat facilitated at such surface temperatures. Over the heating time of 20–40 s, the intensity of O slightly increases, and there is an inflection point at 20 s. Furthermore, the increasing rate of the CN intensity becomes slower. In this period, it is inferred that there exists intense competition between complex chemical reactions, including oxidation, nitridation, and catalysis, which continues to be enhanced with temperature rise. Such phenomena induce further transitions of chemical processes and continuous surface temperature increases. In the final heating period between 40 and 92 s, no significant changes but a slight decrease are observed in the atomic oxygen
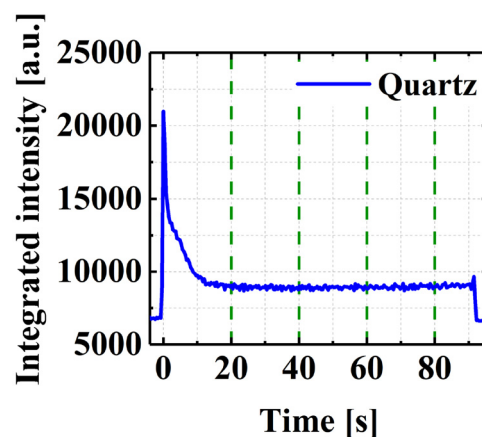

FIG. 9. Time series of the integrated emission intensity of atomic oxygen (777.19 nm) on quartz.
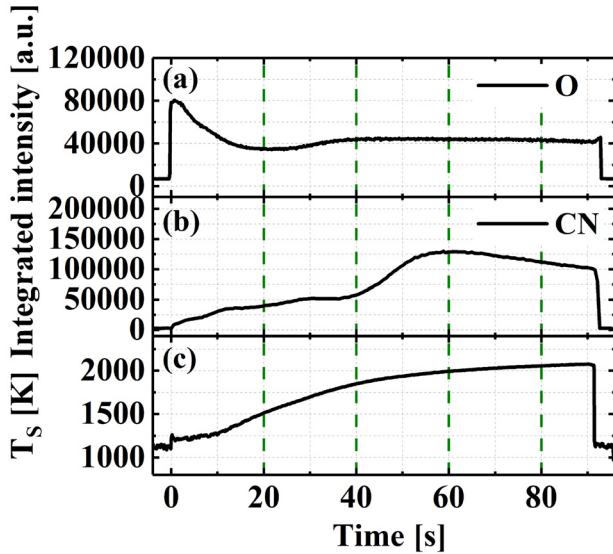
FIG. 10. Time series of the integrated emission intensity of (a) atomic oxygen (777.19 nm), (b) CN, and (c) surface temperature on the C/C composite.

FIG. 11. Dynamic variations of raw data of the laser intensity detected by the LAS system.

intensity, indicating that the consumption of atomic oxygen gradually stabilizes. Whereas for CN, the intensity sharply increases from 40 to 60 s and subsequently decreases over the remaining heating period.

The increasing trend of CN emission intensity indicates that the chemical reactions have turned into the nitridation-dominant process. Since the surface temperature during this period reaches a high value of around 1900 K, the nitridation reaction is substantially enhanced, facilitating production of CN. The decreasing trend might relate to surface recession of the C/C composite (further analyzed in LAS results in Sec. IV C). Finally, the dominant surface chemistry at the OES detection location in the plasma heating can be inferred as shown in Table II:[59,60]

C. Laser absorption spectroscopy

1. Surface profile variations by raw data analysis

Valuable information on surface profile variations is obtained based on the detected laser intensity at the stagnation point ($x = 0$ mm) as shown in Fig. 11. As the sample is inserted into the plasma flow, nearly half of the laser beam is hindered by the sample surface, a corresponding decrease is found in the laser intensity. Within the first 25 s of heating, the profile of the intensity peak gradually decreases, indicating that the surface leading edge gradually swells.
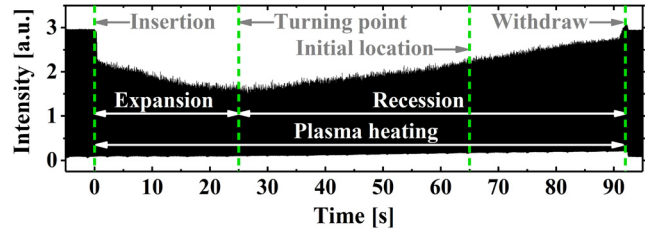
Hence, the detection location of OES is increasingly close to the surface, where the consumption rate of atomic oxygen increases and the measurement solid angle becomes smaller. Such phenomena provide the other two reasons for the abrupt decrease in the O emission intensity (Fig. 10). The surface swelling is the bulk effect of physical characteristics and chemical heat release, as discussed in Sec. IV B 3. During the oxidation and decomposition process, some of the combinations between atomic oxygen and carbon as well as carbon evaporation occur in the inner layer of the composite. Such processes induce the development of pressure in the inner layer of the composite due to the penetration of reaction gaseous products through the fibers. This increasing pressure creates volume expansion in the carbon matrix.[5]

During the 20–30 s interval, a turning point is observed in the laser intensity, which is caused by the intense competition between thermal swelling as well as carbon-consuming and non-consuming reactions (as illustrated in Sec. IV B 3). The intensity begins gradually increasing from 25 s, indicating that the atomic carbon at the leading edge is gradually consumed by nitridation at high surface temperature. Notably, the intensity reaches the initial value after the sample insertion at around 65 s, indicating that the surface leading edge recedes to the initial location. The OES detection point emerges from the sample surface, allowing additional emission signals to be detected. Such phenomena serve as another reason for the sharp increase in the CN emission intensity in the heating period of around 40–60 s. In the remaining heating period, the laser intensity continues to increase, indicating continuous recession of the surface profile. Such process results in the departure of the detection location from the stagnation point where intense chemical reactions occur. Hence, the CN emission quickly decreases over the 60–90 s as shown in Fig. 10. As the sample is drawn out of the plasma flow, the laser intensity nearly reaches the value as before sample insertion, indicating that the test sample experiences surface recession of nearly 0.5 mm within the whole period of plasma heating. Based on the analysis above, raw data provided by

TABLE II. Surface chemistry determined by OES results.

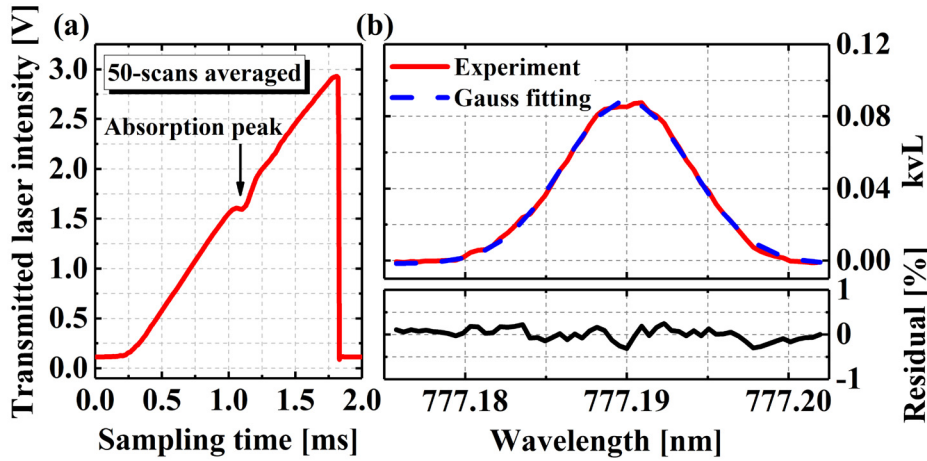| 0–20 s oxidation dominant	20–40 s intense competition	40–60 s nitridation dominant	60–92 s surface recession
(1) $C + O \rightarrow CO$	(1) $C + O \rightarrow CO$	(1) $C + N \rightarrow CN$	(1) $C + N \rightarrow CN$
	(2) $O + O \rightarrow O_2$	(2) $C + N_2 \rightarrow CN + N$	(2) $C + N_2 \rightarrow CN + N$
	(3) $C + N \rightarrow CN$	(3) $CO + N \rightarrow CN + O$	(3) $CO + N \rightarrow CN + O$
	(4) $C + N_2 \rightarrow CN + N$		
	(5) $CO + N \rightarrow CN + O$		

FIG. 12. Representative signal of LAS adjacent to the C/C composite: (a) Transmitted intensity of the laser on the C/C composite; (b) Top: absorption peak, bottom: fitting residual.

LAS detection adds valuable information to the chemical pathways as analyzed by OES.

2. Translational temperature T_{tr} and atomic number density of $O_{777.19\,nm}$ n_O

The representative signal of LAS adjacent to the C/C composite is shown in Fig. 12, which shows a high signal-to-noise ratio and small fitting residual. Details regarding data processing of the LAS method have been presented in our previous work.[41] Quantitative results of T_{tr} and n_O detected by the LAS system are directly presented in Fig. 13 for quartz and Fig. 14 for C/C composite. Using the Taylor series method,[61] the measurement uncertainty of T_{tr} is estimated to be 2.4% (at 5500 K), and the corresponding uncertainty of n_O is estimated to be far below 0.01%.

Analysis regarding chemical reaction mechanisms will be made from the perspective of heat release and reaction processes based on the results of T_{tr} and n_O, respectively. The blue solid line represents the results at the stagnation point ($x = 0$ mm) for quartz, and the red solid line for the C/C composite. In Figs. 13 and 14, the black and cyan dashed lines represent the results at the distance of 1 and 2 mm, respectively, from the sample surface.

For the quartz sample, there are no significant changes among various axial locations, which shows that the chemical activity of quartz is quite low. In Fig. 13(a), T_{tr} at $x = 0$ mm is slightly lower than that at $x = 1$ and 2 mm, this is due to endothermic reactions such as SiO production through Si and SiO_2 oxidation[60] or quartz evaporation at the surface. In Fig. 13(b), the decreasing rate of n_O in the first 20 s decreases slightly from the axial location of $x = 0–2$ mm. This shows that the atomic oxygen exhibits a higher consumption rate when approaching closer to the surface; such trend is ascribed to slightly higher oxidation rate at the surface than that in the boundary layer.

For the C/C composite, the T_{tr} and n_O results exhibit substantial discrepancies in both the axial direction and time series, indicating that there existed complex reactions between the gas and surface. Since the atomic oxygen originated from the coming flow and is substantially excited, T_{tr} is closely related to chemical heating at the boundary layer. The T_{tr} on the C/C composite surface is lower than that on quartz surface, showing that the C/C composite has a higher heat dissipation capability than quartz. Since the rate of heat dissipation through radiation becomes increasingly important at high temperatures,[62] the energy of the gas particles is partially dissipated by radiation, given the high surface temperature of the C/C composite [Fig. 4(b)]. Additionally, the ablative nature of removing the surface C/C layers leads to a further reduction in the heat transfer from the shock layer.[2,3]

In Fig. 14(a), the T_{tr} curve exhibits a decreasing trend in the initial approximately 15–25 s heating time and reaches a local minimum at the end of this first decreasing period. The decreasing trend is due to
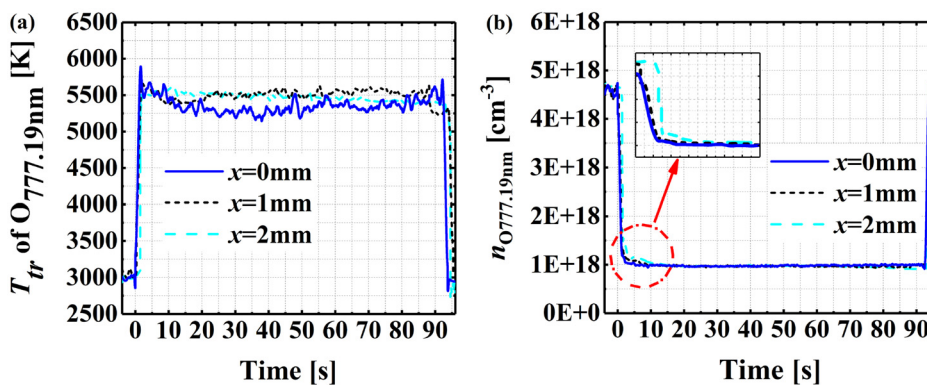

FIG. 13. Temporally and spatially resolved results of (a) T_{tr} and (b) n_O on the quartz surface.
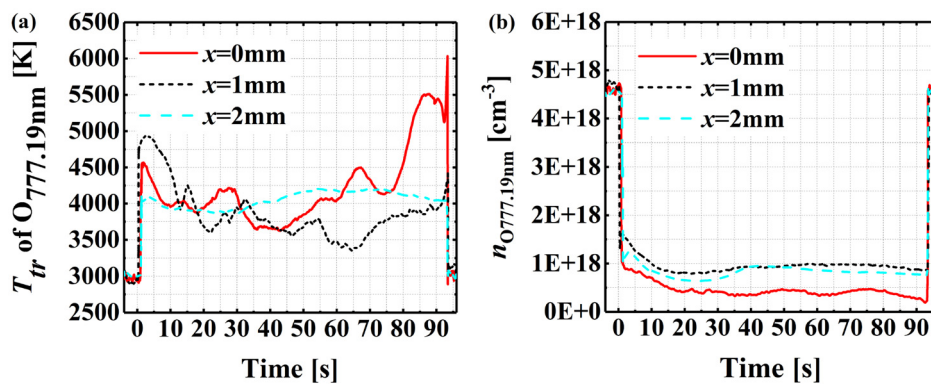
FIG. 14. Temporally and spatially resolved results of (a) T_{tr} and (b) n_O on the C/C composite.

heat dissipation processes such as ablation near the surface. The decreasing rates of T_{tr} became higher from $x = 0$ mm to $x = 2$ mm. Such phenomena relate to surface swelling of the C/C composite. When the surface expands, the detection location is correspondingly closer to the sample surface. Since the heat dissipation rate increases when approaching the surface, the decreasing rate of T_{tr} became higher from $x = 2$ mm to $x = 0$ mm. The axial distribution of T_{tr} shows a similar trend with the literature.[27]

The time points of the first local minimum value of T_{tr} appear at 15, 20, and 25 s for detection locations of $x = 0$, 1, and 2 mm, respectively. These time points show a delay trend with axial locations away from the surface. This shows consistency with the surface swelling and heat dissipation as well as the axial distribution discussed above. In the subsequent heating period, T_{tr} at $x = 0$ and 1 mm experiences a second period of decrease and start to rise at around 40 and 65 s, respectively. The decreasing trend is related to endothermic reactions of nitridation as discussed in Sec. IV B 3. The increasing trend is accounted for surface recession, in which the detection location gradually moves away from the region where there is intense nitridation. The remaining trend at $x = 2$ mm conforms to the surface profile variations. T_{tr} continues to increase until around 40 s when the chemical reaction process propagates into nitridation, in which period the consumption rate of the atomic oxygen becomes lower compared to that in the oxidation period. Due to this transition, the laser intensity in Fig. 11 suppresses the initial value at around 60 s when the surface recedes back to the initial location and remains stable in the remaining heating period with the surface recession. Such phenomena indicate that the gas–surface interactions gradually attenuate at around 2 mm away from the surface.

In Fig. 14(b), n_O experiences an abrupt increase from $x = 0$ mm to $x = 1$ mm in the axial direction, showing that the consumption rate of atomic oxygen increases with decreasing distance from the surface. Additionally, n_O sees a similar decrease within the first around 20 s as the radiance profile shown in Fig. 10, which can be explained by the surface swelling as discussed above. Additionally, n_O at the stagnation point ($x = 0$ mm) exhibits more turning points than that at $x = 1$ mm and $x = 2$ mm, indicating that atomic oxygen is involved in more-competitive processes closer to the surface. These phenomena quantitatively reflect the axial distributions in reaction complexity.

Based on quantitative results from LAS presented above, the chemical behavior of atomic oxygen is distinguished from highly coupled physico-chemical processes. The axial distributions and dynamic behavior of the translational temperature and number density play a pivotal role in characterizing the chemical processes and their correspondence to surface variations on a microscopic scale.

V. CONCLUSIONS

Quantitative molecular-scale insights into the gas–surface interactions on C/C composite have been achieved by OES and LAS in this work. Experiments are conducted on a large-scale ICP wind tunnel with a stagnation enthalpy of 20.08 MJ/kg. Samples are heated for around 100 s by the air plasma. Based on the dynamic variations of the emission intensity and spectral structure recorded by OES, chemical reaction mechanisms and the thermal nonequilibrium are analyzed. Additionally, the translational temperature and number density of atomic oxygen in the boundary layer with high temporal and spatial resolution are quantified by LAS. Variations of these two parameters exhibit a close correspondence to surface swelling and recession process depicted by the laser intensity, which distinguishes the heat release and atomic consumption caused by chemical reactions from highly coupled physico-chemical processes. Finally, reaction mechanisms (sequentially dominated by oxidation, intense competition, nitridation, and surface recession) have been extracted combining the spectral and traditional results. These results show that the spectral insights have the potential to connect the macroscopic observables with microscopic behavior.

In future studies, spectral insights will be extended to higher-dimensional, and multi-species detection. To visualize the structure of the reactive flow at the interface, high speed imaging (to capture two-dimensional images) and multi-view imaging (to reconstruct the three-dimensional structure of the flow field) will be implemented. For more details of the chemical mechanisms, diagnostics of more species that are related to chemical reactions (such as CO, C_1, C_2, and C_3) will be simultaneously applied to the high-temperature interface. Experiments that detect a wide range of surface temperatures will be conducted to investigate gas–surface interactions under various flight conditions. Furthermore, deeper analysis on thermal nonequilibrium will be conducted by combining spatially resolved experimental results with simulations.

ACKNOWLEDGMENTS

AUTHOR DECLARATIONS

Conflict of Interest

The authors have no conflicts to disclose.

Author Contributions

Sihan Fang: Data curation (equal); Formal analysis (equal); Investigation (equal); Methodology (equal); Visualization (equal); Writing – original draft (equal). **Xin Lin:** Conceptualization (equal); Funding acquisition (equal); Methodology (equal); Project administration (equal); Supervision (equal). **Junna Yang:** Investigation (equal). **Hui Zeng:** Investigation (equal). **Xingying Zhu:** Investigation (equal). **Fa Zhou:** Investigation (equal). **Dongbin Ou:** Funding acquisition (equal); Project administration (equal). **Fei Li:** Funding acquisition (equal); Methodology (equal). **Xilong Yu:** Funding acquisition (equal).

DATA AVAILABILITY

The data that support the findings of this study are available within the article.

REFERENCES

[1] Q. Zhu, C. Zhang, and W. Yang, "The influence of permeability on the ablation process for an ablative material," Fractals **27**, 1950105 (2019).

[2] K. S. Gopalan, A. Borner, J. C. Ferguson, F. Panerai, N. N. Mansour, and K. A. Stephani, "Gas–surface interactions in lightweight fibrous carbon materials," Comput. Mater. Sci. **205**, 111190 (2022).

[3] O. Uyanna and H. Najafi, "Thermal protection systems for space vehicles: A review on technology development, current challenges and future prospects," Acta Astronaut. **176**, 341 (2020).

[4] E. L. Reynolds, A. Driesman, J. Kinnison, and M. K. Lockwood, "Solar probe plus mission overview," AIAA Paper No. 2013-4879, 2013.

[5] P. Sanoj and K. Balasubramanian, "Hybrid carbon-carbon ablative composites for thermal protection in aerospace," J. Compos. **2014**, 825607.

[6] C. R. Alba, R. B. Greendyke, S. W. Lewis, R. G. Morgan, and T. J. McIntyre, "Numerical modeling of Earth reentry flow with surface ablation," J. Spacecr. Rockets **53**, 84–97 (2015).

[7] X. Zhang, B. Du, P. Hu, Y. Cheng, and J. Han, "Thermal response, oxidation and ablation of ultra–high temperature ceramics, C/SiC, C/C, graphite and graphite–ceramics," J. Mater. Sci. Technol. **102**, 137–158 (2022).

[8] S. Meng, Y. Zhou, W. Xie, F. Yi, and S. Du, "Multiphysics coupled fluid/thermal/ablation simulation of carbon/carbon composites," J. Spacecr. Rockets **53**, 930–935 (2016).

[9] B. Vancrayenest and D. Fletcher, "Ablation of carbonaceous heatshields: Spectroscopic emission survey in a subsonic ICP flow," AIAA Paper No. 2008-3911, 2008.

[10] B. Helber, A. Turchi, J. B. Scoggins, A. Hubin, and T. E. Magin, "Experimental investigation of ablation and pyrolysis processes of carbon-phenolic ablators in atmospheric entry plasmas," Int. J. Heat Mass Transfer **100**, 810–824 (2016).

[11] U. A. Sheikh, H. Wei, S. W. Lewis, C. M. James, P. Leyland, R. G. Morgan, and T. J. McIntyre, "Spectrally filtered imaging and vacuum ultraviolet spectroscopy of preheated models in X2," AIAA J. **55**, 4167–4180 (2017).

[12] L. Shakurova, I. Armenise, and E. Kustova, "State-specific slip boundary conditions in non-equilibrium gas flows: Theoretical models and their assessment," Phys. Fluids **35**, 086109 (2023).

[13] M. Yu, Z. Qiu, and Y. Takahashi, "Numerical investigation of surface catalytic effect on the plasma sheath of a hypersonic re-entry capsule," Phys. Fluids **35**, 056106 (2023).

[14] Z. Cui, Z. Ye, J. Zhao, X. Sun, G. Yao, and D. Wen, "Coupled surface-volume pyrolysis effects of carbon-phenolic resin composites under hyperthermal non-equilibrium flows," Phys. Fluids **34**, 062117 (2022).

[15] H. Shim, S. Lee, J. G. Kim, and G. Park, "CO2 number density measurement in a shock tube with preheated carbon surface," Phys. Fluids **34**, 067105 (2022).

[16] S. Lee and J. G. Kim, "Stagnation-point heating and ablation analysis of orbital re-entry experiment," Phys. Fluids **33**, 086102 (2021).

[17] Z. Cui, J. Zhao, L. He, H. Jin, J. Zhang, and D. Wen, "A reactive molecular dynamics study of hyperthermal atomic oxygen erosion mechanisms for graphene sheets," Phys. Fluids **32**, 112110 (2020).

[18] V. I. Lysenko, S. A. Gaponov, B. V. Smorodsky, A. D. Kosinov, and M. I. Yaroslavtsev, "Influence of surface sublimation on the stability of the supersonic boundary layer and the laminar–turbulent transition," Phys. Fluids **33**, 024101 (2021).

[19] M. G. D'Souza, T. N. Eichmann, D. F. Potter, R. G. Morgan, T. J. McIntyre, P. A. Jacobs, and N. R. Mudford, "Observation of an ablating surface in expansion tunnel flow," AIAA J. **48**, 1557–1560 (2010).

[20] G. L. Vignoles, A. Turchi, D. Bianchi, P. Blaineau, X. Lamboley, D. Le Quang Huy, C. Levet, O. Caty, and O. Chazot, "Ablative and catalytic behavior of carbon-based porous thermal protection materials in nitrogen plasmas," Carbon **134**, 376–390 (2018).

[21] J. M. Meyers, W. P. Owens, and D. G. Fletcher, "Experimental strategy to determine nitrogen catalytic behavior of high-temperature woven ceramics," J. Am. Ceram. Soc. **103**, 4536–4547 (2020).

[22] D. Cinquegrana, R. Votta, C. Purpura, and E. Trifoni, "Continuum breakdown and surface catalysis effects in NASA arc jet testing at SCIROCCO," Aerosp. Sci. Technol. **88**, 258–272 (2019).

[23] E. J. Fahy, "Superorbital re-entry shock layers: Flight and laboratory comparisons," Ph.D. thesis (School of Mechanical and Mining Engineering, Brisbane, 2017).

[24] B. Erzincanli, C. Asma, and O. Chazot, "Ablative material testing at VKI plasmatron facility," AIAA Paper No. 2010-4511, 2010.

[25] C. Levet, B. Helber, J. Couzi, J. Mathiaud, J. B. Gouriet, O. Chazot, and G. L. Vignoles, "Microstructure and gas-surface interaction studies of a 3D carbon/carbon composite in atmospheric entry plasma," Carbon **114**, 84–97 (2017).

[26] L. Pietanza, O. Guaitella, V. Aquilanti, I. Armenise, A. Bogaerts, M. Capitelli, G. Colonna, V. Guerra, R. Engeln, E. Kustova, A. Lombardi, F. Palazzetti, and T. Silva, "Advances in non-equilibrium CO_2 plasma kinetics: A theoretical and experimental review," Eur. Phys. J. D **75**, 237 (2021).

[27] R. Ravichandran, S. W. Lewis, C. M. James, R. G. Morgan, and T. J. McIntyre, "Graphite ablation and radiation interaction with hypervelocity Earth-entry flows," J. Thermophys. Heat Transfer **35**, 335–348 (2020).

[28] M. MacDonald and C. O. Laux, "Experimental characterization of ablation species in an air plasma ablating boundary layer," AIAA Paper No. 2014-2251, 2014.

[29] J. M. Meyers and D. G. Fletcher, "Nitrogen surface catalyzed recombination efficiency from two-photon laser induced fluorescence measurements," J. Thermophys. Heat Transfer **33**, 128–138 (2018).

[30] D. G. Fletcher and J. M. Meyers, "Surface catalyzed reaction efficiencies in oxygen plasmas from laser-induced fluorescence measurements," J. Thermophys. Heat Transfer **31**, 410–420 (2016).

[31] R. K. Hanson, "Applications of quantitative laser sensors to kinetics, propulsion and practical energy systems," Proc. Combust. Inst. **33**, 1–40 (2011).

[32] P. Werle, "A review of recent advances in semiconductor laser based gas monitors," Spectrochim. Acta, Part A **54**, 197–236 (1998).

[33] Z. Du, Z. Shuai, J. Li, N. Gao, and T. Kebin, "Mid-infrared tunable laser-based broadband fingerprint absorption spectroscopy for trace gas sensing: A review," Appl. Sci. **9**, 338 (2019).

[34] H. Burghaus, C. F. Kaiser, A. S. Pagan, S. Fasoulas, and G. Herdrich, "Aerothermodynamic characterization of an inductively generated CO_2 plasma by laser absorption spectroscopy," AIAA Paper No. 2022-1617, 2022.

[35] L. Shao, B. Fang, F. Zheng, X. Qiu, Q. He, J. Wei, C. Li, and W. Zhao, "Simultaneous detection of atmospheric CO and CH_4 based on TDLAS using a single 2.3 μm DFB laser," Spectrochim. Acta, Part A **222**, 117118 (2019).

[36] S. Fang, Z. Wang, X. Lin, F. Li, R. Li, J. Li, Z. Zhang, Y. Liu, and X. Yu, "Characterizing combustion of a hybrid rocket using laser absorption spectroscopy," Exp. Therm. Fluid Sci. **127**, 110411 (2021).

[37]Z. Wang, X. Lin, F. Li, J. Peng, Y. Liu, Z. Zhang, S. Fang, and X. Yu, "Determining the time-resolved mass flow rates of hybrid rocket fuels using laser absorption spectroscopy," Acta Astronaut. **188**, 110–120 (2021).

[38]I. A. Schultz, C. S. Goldenstein, J. B. Jeffries, R. K. Hanson, R. D. Rockwell, and C. P. Goyne, "Diode laser absorption sensor for combustion progress in a model scramjet," J. Propul. Power **30**, 550–557 (2014).

[39]K. Sun, R. Sur, X. Chao, J. B. Jeffries, R. K. Hanson, R. J. Pummill, and K. J. Whitty, "TDL absorption sensors for gas temperature and concentrations in a high-pressure entrained-flow coal gasifier," Proc. Combust. Inst. **34**, 3593–3601 (2013).

[40]J. Wu, H. Zheng, Y. Wang, Q. Cao, F. Zhou, J. Zhang, and X. Huang, "Experimental diagnosis of electron density and temperature in capacitively coupled argon plasmas: Triple-frequency discharges and two-dimensional spatial distributions," Phys. Plasmas **28**, 093501 (2021).

[41]S. Fang, X. Lin, H. Zeng, X. Zhu, F. Zhou, J. Yang, F. Li, D. Ou, and X. Yu, "Gas–surface interactions in a large-scale inductively coupled plasma wind tunnel investigated by emission/absorption spectroscopy," Phys. Fluids **34**, 082113 (2022).

[42]L. He, Z. Cui, X. Sun, J. Zhao, and D. Wen, "Sensitivity analysis of the catalysis recombination mechanism on nanoscale silica surfaces," Nanomaterials **12**, 2370 (2022).

[43]X. Lin, L. Z. Chen, J. P. Li, F. Li, and X. L. Yu, "Experimental and numerical study of carbon-dioxide dissociation for mars atmospheric entry," J. Thermophys. Heat Transfer **32**, 503–513 (2018).

[44]See http://webbook.nist.gov/chemistry/ for National Institute of Standards and Technology: NIST Chemistry WebBook.

[45]M. Nations, S. Wang, C. S. Goldenstein, K. Sun, D. F. Davidson, J. B. Jeffries, and R. K. Hanson, "Shock-tube measurements of excited oxygen atoms using cavity-enhanced absorption spectroscopy," Appl. Opt. **54**, 8766–8775 (2015).

[46]S. Löhle, C. Eichhorn, A. Steinbeck, S. Lein, G. Herdrich, H.-P. Röser, and M. Auweter-Kurtz, "Oxygen plasma flow properties deduced from laser-induced fluorescence and probe measurements," Appl. Opt. **47**, 1837–1845 (2008).

[47]M. Matsui, K. Komurasaki, G. Herdrich, and M. Auweter-Kurtz, "Enthalpy measurement in inductively heated plasma generator flow by laser absorption spectroscopy," AIAA J. **43**, 2060–2064 (2005).

[48]M. Nations, L. S. Chang, J. B. Jeffries, R. K. Hanson, M. E. MacDonald, A. Nawaz, J. S. Taunk, T. Gökçen, and G. Raiche, "Characterization of a large-scale arcjet facility using tunable diode laser absorption spectroscopy," AIAA J. **55**, 3757–3766 (2017).

[49]S. S. Harilal, B. E. Brumfield, N. L. LaHaye, K. C. Hartig, and M. C. Phillips, "Optical spectroscopy of laser-produced plasmas for standoff isotopic analysis," Appl. Phys. Rev. **5**, 021301 (2018).

[50]C. Aragón and J. A. Aguilera, "Characterization of laser induced plasmas by optical emission spectroscopy: A review of experiments and methods," Spectrochim. Acta, Part B **63**, 893–916 (2008).

[51]F. Iza and J. A. Hopwood, "Rotational, vibrational, and excitation temperatures of a microwave-frequency microplasma," IEEE Trans. Plasma Sci. **32**, 498–504 (2004).

[52]T. Hermann, S. Löhle, U. Bauder, R. Morgan, H. Wei, and S. Fasoulas, "Quantitative emission spectroscopy for superorbital reentry in expansion tube X2," J. Thermophys. Heat Transfer **31**, 257–268 (2017).

[53]J. D. Anderson, Jr., *Hypersonic and High-Temperature Gas Dynamics* (American Institute of Aeronautics and Astronautics, Inc., 2006).

[54]X. Lin, D. B. Ou, J. L. Peng, H. Zeng, F. Li, and X. L. Yu, "Cooling-water leakage diagnosis using optical emission spectroscopy for a large-scale arc-heated facility," J. Thermophys. Heat Transfer **33**, 900–906 (2019).

[55]C. O. Laux, "Optical dignostics and radiative emission of air plasmas," Ph.D. thesis (Department of Mechanical Engineering, California, 1993).

[56]G. Colonna and M. Capitelli, "A few level approach for the electronic partition function of atomic systems," Spectrochim. Acta, Part B **64**, 863–873 (2009).

[57]Z. Remes, A. Kromka, J. Micova, B. Rezek, A. Poruba, and H.-S. Hsu, "Optical emission spectroscopy of radio frequency inductively coupled plasma for cold hydrogenation of nanoparticles," IOP Conf. Ser.: Mater. Sci. Eng. **1050**, 012012 (2021).

[58]X. Lin, X.-L. Yu, F. Li, S.-H. Zhang, J.-G. Xin, and X.-Y. Zhang, "Measurements of non-equilibrium and equilibrium temperature behind a strong shock wave in simulated martian atmosphere," Acta Mech. Sin. **28**, 1296–1302 (2012).

[59]C. Park, J. T. Howe, R. L. Jaffe, and G. V. Candler, "Review of chemical-kinetic problems of future NASA missions. II - Mars entries," J. Thermophys. Heat Transfer **8**, 9–23 (1994).

[60]H. Hald, "Operational limits for reusable space transportation systems due to physical boundaries of C/SiC materials," Aerosp. Sci. Technol. **7**, 551–559 (2003).

[61]W. C. Hugh and W. S. Glenn, *Experimentation, Validation, and Uncertainty Analysis for Engineers* (John Wiley & Sons, 2018).

[62]A. Pagan, B. Massuti-Ballester, and G. Herdrich, "Total and spectral emissivities of demising aerospace materials," Front. Appl. Plasma Technol. **9**, 7 (2016).

08 April 2024 02:59:17